Pergamon

Int. J. Heat Mass Transfer. Vol. 37, No. 6, pp. 885–892, 1994
Elsevier Science Ltd

0017–9310/94 $6.00+0.00

0017–9310(93)E0018–C

Oscillations in thermocapillary convection in a square cavity†

MICHAEL KANOUFF
Sandia National Laboratories, Livermore, CA 94550, U.S.A.

and

RALPH GREIF
University of California, Berkeley, CA 94720, U.S.A.

(*Received* 14 *April* 1993 *and in final form* 22 *October* 1993)

Abstract—The governing equations for momentum and energy transport have been solved for the thermocapillary flow in a differentially heated square cavity. The fluid was assumed to contain a surface active impurity such that the surface tension was a quadratic function of the temperature where the maximum surface tension occurs at the mean cavity temperature. A Prandtl number of 0.1 was used because the primary interest here is for liquid metals. For low Marangoni numbers the flow was steady, stable and symmetric about the center vertical plane and consisted of two opposing vortices. For Marangoni numbers above 1200 the flow, given an initial disturbance, was oscillatory and in a periodic steady state.

1. INTRODUCTION

FLOWS induced by surface tension gradients (Marangoni flows) occur in the processing of materials where small amounts of material are melted and allowed to resolidify; common examples include welding and crystal growth operations. In these processes large temperature differences are created in small amounts of liquid which have a large free surface area to volume ratio. The surface tension gradients resulting from the large temperature differences in the liquid can produce fluid velocities as large as one meter per second. The flow affects solute distributions and crystal structure in the re-solidified material and weld penetration. The effects of Marangoni flows are complex and variable because the surface tension is affected by small amounts of surface active impurities, e.g. sulfur in molten steel. The concentrations of impurities often vary with materials which alters the Marangoni flow and its effects on the product material. These effects make it extremely difficult to control or predict the properties of the finished product.

Experimental studies of flows in small liquid volumes have exhibited a transition from a steady to an oscillatory state. Hurle *et al.* [1] measured temperatures in flows of molten gallium ($Pr = 0.02$) that were contained in open rectangular boats and heated from one side. Temperatures were found to oscillate for boat temperature differences above a critical value which depended on the dimensions of the boat. Schwabe and Scharmann [2] measured temperature oscillations in sodium nitrate ($Pr = 9$) in a cylindrical floating zone suspended between the ends of two coaxial cylinders where the upper cylinder was heated. The onset of the oscillations occurred at a critical Marangoni number (Ma_c) approximately equal to 1.6×10^4. They pointed out that the onset of oscillations in a floating zone as measured by Chun and Wuest [3] in methyl alcohol ($Pr = 7$) also coincided with a Marangoni number of this order of magnitude and that the onset of oscillations in the open boat experiment in ref. [1] occurred for $Ma = 2 \times 10^3$. Chun and Wuest [4] investigated methyl alcohol ($Pr = 7$) in a floating zone. They measured temperature oscillations ($Ma_c = 1.4 \times 10^4$) and simultaneously visualized the oscillating flow with a 'light-cut' technique. The flow visualization revealed an asymmetrical oscillating flow pattern. Kamotani *et al.* [5] measured temperature oscillations in floating zones of hexadecane ($Pr = 0.09$) and Fluorinert ($Pr = 0.11$) (3M Co.) with the onset of oscillations occurring at Marangoni numbers approximately equal to 2×10^4.

Smith and Davis [6] performed a stability analysis of a planar liquid layer subject to an imposed constant temperature gradient parallel to the free surface. A linear variation of the surface tension with temperature was specified. A parallel return flow solution to the momentum and energy equations was used as the basic state. The three dimensional disturbance equations were solved and an oscillatory instability in the form of oblique hydrothermal waves was obtained for $Pr < 0.6$. Ma_c decreased for decreasing Pr.

Carpenter and Homsy [7] studied two dimensional thermocapillary flows in square cavities with a nondeformable free surface. Surface tension was assumed

†This work was supported by the U.S. Department of Energy under contract No. DE-AC04-76DP00789.

NOMENCLATURE

c_p specific heat
$\mathbf{e}_x, \mathbf{e}_y, \mathbf{e}_z$ unit vectors in the coordinate directions
$\mathbf{F}_{net\ visc}$ net tangential force acting on the boundaries of the fluid
$\mathbf{F}_{L\ visc}$ net tangential boundary force acting on the left vortex
$\mathbf{F}_{R\ visc}$ net tangential boundary force acting on the right vortex
k thermal conductivity
L length of a side of the square domain
Ma Marangoni number, $\gamma_T \Delta T \rho c_p L/(\mu k)$
Pr Prandtl number, $\mu c_p/k$
t time
T temperature
$\mathbf{V}$ the velocity vector
V_c the velocity scale, $\gamma_T \Delta T/\mu$
x, y the horizontal and vertical coordinates, respectively
X_0 the location of the dividing streamline between the vortices (at $y^* = 1$).

Greek symbols
γ surface tension
γ_T the maximum value of $d\gamma/dT$
μ dynamic viscosity
ρ density
ψ stream function
ω vorticity, $\mathbf{e}_z \cdot \nabla \times \mathbf{V}$.

Subscripts and superscripts
* dimensionless quantities
L, R left, right vortices.

to decrease linearly with temperature. A wide range of values of Pr was considered along with Marangoni numbers exceeding 10^5. A linear stability analysis showed that the flows were stable to a restricted class of disturbances. They concluded that oscillations in thermocapillary flows must include modes with either three-dimensional effects or free surface deformations, or both of these elements simultaneously.

In the stability analyses cited, the rate of change of surface tension with temperature was assumed to be a constant. This is often a good assumption for pure liquids, where surface tension is a maximum at the fusion temperature and monotonically decreases as the temperature increases towards the critical temperature. However, if a surface active element is present the variation of the surface tension with temperature is more complex. Sahoo *et al.* [8] determined the effects of small concentrations of surfactants on the surface tension of liquids. For low temperatures, the concentration of the surfactant on the surface may be large which results in a smaller surface tension. As the temperature increases, the surfactant is driven off the surface; the surface tension then increases until the surface concentration is sufficiently low that the surface tension dependence on temperature becomes similar to that of a pure liquid. Thus, when an impurity is present, the rate of change of surface tension with temperature can be positive for low temperatures and negative for high temperatures.

In the present work, thermocapillary flow in a two dimensional differentially heated square cavity with a non-deformable free surface is studied. A quadratic function of temperature was used for the surface tension to study the effects of surface active impurities; e.g. sulfur, that may exist in small concentrations in otherwise pure liquids such as molten steel. For these conditions the rate of change of surface tension with temperature, is positive for low temperatures and is negative for high temperatures [8]. Unlike the flows previously studied [6, 7], the two dimensional flow studied here was found to be unstable to asymmetric two dimensional disturbances and to be oscillatory and periodic for Marangoni numbers larger than approximately 1200.

2. PROBLEM DEFINITION

In this section the governing equations are presented for the model problem proposed by Zebib *et al.* [9] for flow in a differentially heated square cavity driven by thermocapillary forces. The case considered here is for a fluid containing a surface active impurity, with the surface tension varying as a quadratic function of the temperature.

The governing equations, in vorticity–stream function form, are scaled as in Zebib *et al.* [9]. Length, time, stream function and vorticity are scaled by L, L/V_c, LV_c and V_c/L, respectively. L is the length of the cavity walls and V_c is a velocity scale given by $\gamma_T \Delta T/\mu$, where γ_T is a surface tension parameter discussed below and ΔT is the temperature difference across the cavity. The temperature is scaled as $T^* = (T - T_0)/\Delta T$, where T is the dimensional temperature. The conservation equations are given by:

$$\frac{\partial T^*}{\partial t^*} + \nabla^* \cdot (T^* \mathbf{V}^*) = \frac{1}{Ma} \nabla^{*2} T^* \tag{1}$$

$$\frac{\partial \omega^*}{\partial t^*} + \nabla^* \cdot (\omega^* \mathbf{V}^*) = \frac{Pr}{Ma} \nabla^{*2} \omega^* \tag{2}$$

$$\omega^* = \nabla^{*2} \psi^* \tag{3}$$

where $\omega^* = \mathbf{e}_z \cdot \nabla^* \times \mathbf{V}^*$ is the vorticity, $Ma = \gamma_T \Delta T \rho c_p L/(k\mu)$ is the Marangoni number and $Pr =$

$\mu c_p/k$. The fluid velocity vector, $\mathbf{V}^*$, is written in terms of the stream function according to:

$$\mathbf{V}^* = -\frac{\partial \psi^*}{\partial y^*}\mathbf{e}_x + \frac{\partial \psi^*}{\partial x^*}\mathbf{e}_y. \quad (4)$$

The boundary conditions are:

$$\psi^* = 0, \quad \frac{\partial \psi^*}{\partial x^*} = 0, \quad T^* = 1 \quad x^* = 0, \quad (5a, b, c)$$

$$\psi^* = 0, \quad \frac{\partial \psi^*}{\partial x^*} = 0, \quad T^* = 0 \quad x^* = 1, \quad (6a, b, c)$$

$$\psi^* = 0, \quad \frac{\partial \psi^*}{\partial y^*} = 0, \quad q^* = 0 \quad y^* = 0, \quad (7a, b, c)$$

$$\psi^* = 0, \quad \omega^* = -\frac{d\gamma^*}{dT^*}\frac{dT^*}{dx^*}, \quad q^* = 0 \quad y^* = 1. \quad (8a, b, c)$$

The temperature T_0 is specified on the right vertical wall and the higher temperature, $T_0+\Delta T$, is on the left wall. The bottom and top surfaces are adiabatic. The no-slip condition is applied to the bottom and sides of the cavity. The upper free surface is assumed to remain flat and subject to the tangential forces of surface tension and viscous shear.

Equations (9a, b) are used to approximate the results given by Sahoo *et al.* [8] for the surface tension and its derivative, as a function of temperature:

$$\gamma^* = T^* - T^{*2}, \quad \frac{d\gamma^*}{dT^*} = (1-2T^*). \quad (9a, b)$$

The surface tension is scaled according to $\gamma^* = (\gamma-\gamma_0)/(\Delta T\gamma_T)$ where γ_0 is the value of the surface tension at the temperature, T_0. According to equation (9a), the maximum surface tension occurs at the mean cavity temperature. γ_T is the maximum value of $d\gamma/dT$ for the temperature range considered here. Equations (9a, b) are present in Fig. 1 along with the results of Sahoo *et al.* [8] for molten steel with sulfur as an impurity at a concentration of 30 p.p.m. For the Fe–S system, their results give $\gamma = 1229$ dyne cm^{-1} and $d\gamma/dT = 0.332$ dyne cm^{-1} °C^{-1} for a temperature of 1536°C. In Fig. 1 their results were normalized using these values for γ_0, γ_T and T_0, respectively, and ΔT was set equal to 1400°C. Both the results of Sahoo *et al.* [8] and the quadratic formulation give both positive and negative values for $d\gamma/dT$ and the variation with temperature is roughly anti-symmetric about $T^* = 0.5$.

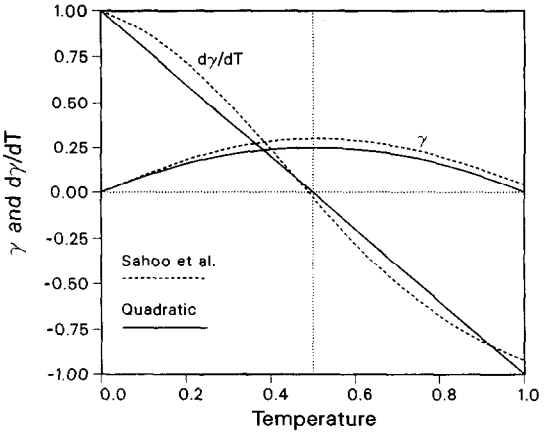

FIG. 1. The non-dimensional surface tension and derivative of surface tension with respect to temperature vs temperature from Sahoo *et al.* [8] and for a quadratic formulation.

3. SOLUTION METHOD

The integral forms of the governing equations are obtained by integrating equations (1)–(3) over control volumes; the divergence theorem is used to replace volume integrals of the divergence of a vector with the area integral of the normal component of the vector. Central finite difference expressions are used to represent the diffusion terms and the values of the advection terms at the control volume surfaces are determined by linear interpolation. The adiabatic boundary conditions for the energy equation are incorporated by applying the integral form of the energy equation to half size control volumes surrounding the boundary grid points. The advection and diffusion terms are integrated over the three control volume faces that are interior to the domain only, and no energy enters the remaining control volume face that is on the upper (equation (8c)) or lower (equation (7c)) boundary of the domain. The no-slip condition is applied by using the conditions placed on the first derivative of ψ with respect to the normal to the wall (equations (5b), (6b) and (7b)) and developing second order expressions for the vorticity, as discussed by Raithby and Torrance [10]. Time integration is accomplished using the alternating direction implicit (ADI) method where the tridiagonal matrix algorithm is used. The stream function equation is solved directly using LDU decomposition. The calculations were carried out on a CRAY XMP.

A non-uniform grid was used for most of the calculations where the grid spacing in the vertical direction was reduced such that finer spacing was obtained near the surface and the grid spacing in the horizontal direction was varied such that the finest grid spacing was obtained at the center of the domain. The change in spacing was controlled by the factors R_y and R_x where R_y is the ratio of two successive grid spacings in the vertical direction, $R_y = \Delta y_{i,j+1}/\Delta y_{i,j}$, and R_x is the ratio of two successive grid spacings in the horizontal direction, $R_x = \Delta x_{i+1,j}/\Delta x_{i,j}$ for $x < 0.5$, and $R_x = \Delta x_{i,j}/\Delta x_{i+1,j}$, for $x \geq 0.5$. Most of the calculations were done on a grid with 41 points in the x direction and 31 points in the y direction where $R_y = 0.95$ and $R_x = 0.92$. Calculations were also repeated for the largest value of Ma considered (2000), with a finer grid (61×51) where $R_y = 0.97$ and $R_x = 0.95$. Very good agreement between the results

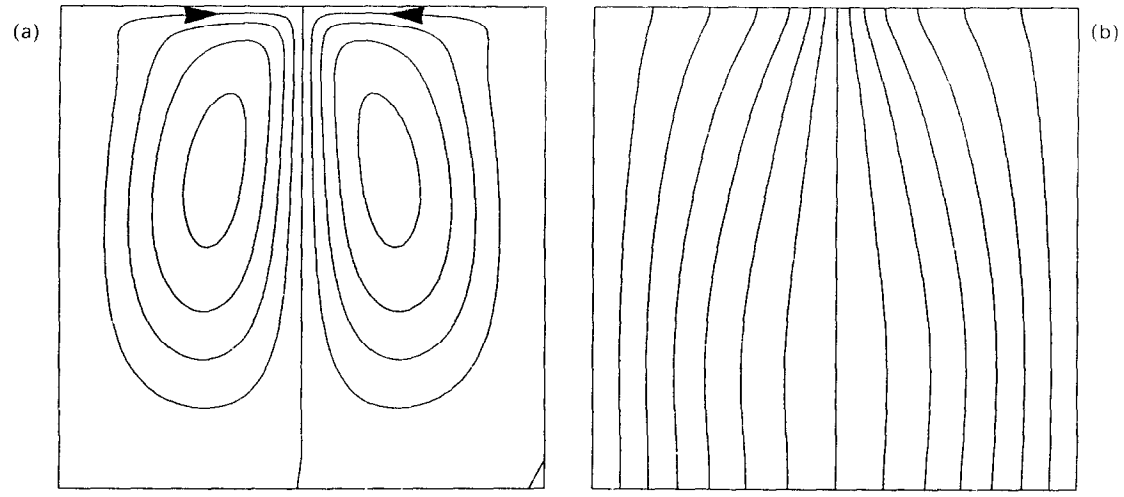

FIG. 2. Steady state streamline (a) and temperature (b) contours for $Ma = 1000$. Streamline and temperature contours are in increments of 1.59×10^{-4} and 0.0714, respectively.

was obtained for the two grid sizes. Specifically, the differences in the maximum velocity (located on the free surface), the maximum value of the stream function and the period of the oscillation were 8, 3 and 1%, respectively.

4. RESULTS

The initial conditions for the calculations were a linear function of x^* for the temperature and a zero value for the fluid velocity. The unsteady development of the temperature and flow fields to a steady state was calculated. The steady solutions were tested for stability by introducing a perturbation to the temperature on the left side of the upper surface. The perturbation, T_p^*, was given by $T_p^* = A_p^* x^*(x^* - 0.5)$, for $(0 < x^* < 0.5)$, and $T_p^* = 0$, for $x^* \geqslant 0.5$. T_p^* was added to the steady result for the temperature on the surface, and then the calculations were continued until either the flow was again steady, or until periodic motion was established. A_p^* was varied from 0.1 to 0.5 to test the dependence of the ensuing response of the flow and temperature fields on the perturbation.

Calculations were carried out for $Pr = 0.1$ and a range of values of Ma from 1000 to 2000. Starting from the stagnant flow conditions, the flow and temperature fields developed into a steady state for $Ma = 1000$ as shown in Fig. 2. In contrast to the results obtained by Zebib *et al.* [9] for $d\gamma^*/dT^*$ equal to a negative constant, the present results for both the flow and temperature fields are symmetric about the line $x^* = 0.5$ (note that the symmetry for the temperature field holds only for the shape of the temperature contours, not for their values). For the case considered here the flow consists of two counter rotating vortices, and the flow direction on the surface is towards the center, $x^* = 0.5$. This is because the surface tension is a maximum at the mean cavity temperature which for this steady solution is located at the center of the surface. After obtaining the steady solution shown in Fig. 2, the perturbation, T_p^* with $A_p^* = 0.5$, was introduced and the calculations were continued. For $Ma = 1000$, the effects of the perturbation diminished and the flow and temperature fields returned to the steady symmetric states shown in Fig. 2.

For $Ma = 2000$, the unperturbed solution again came to a steady symmetric state similar to that shown in Fig. 2 for $Ma = 1000$. Again the asymmetric perturbation, T_p^*, was added to the steady temperature field.† Following a short transition period, the ensuing response was now found to consist of periodic oscillations. Different values for A_p^*, between 0.1 and 0.5, affected the time interval for the transition period, but did not affect the frequency, amplitude or form of the fully developed periodic oscillations. The streamlines for different states spanning one half of the period of the fully developed motion (the other half is similar) are shown in Fig. 3. Figure 3(a) shows two vortices of unequal size, where the vortex on the left is close to its minimum size during the course of the oscillations and the vortex on the right is close to its maximum size. Following this state the left vortex increases in size while the right vortex decreases in size. Fig. 3(b) shows the vortex on the left after it has increased in size such that it fills a large portion of the cavity while the right vortex is reduced in size. The right vortex then begins to collapse as shown in Fig. 3(c), i.e. the dividing streamline is moving from the left wall toward the right wall. Figure 3(d) shows the

† Note that a calculation using a symmetric perturbation was also carried out, and the results showed that the flow returned to the steady symmetric state.

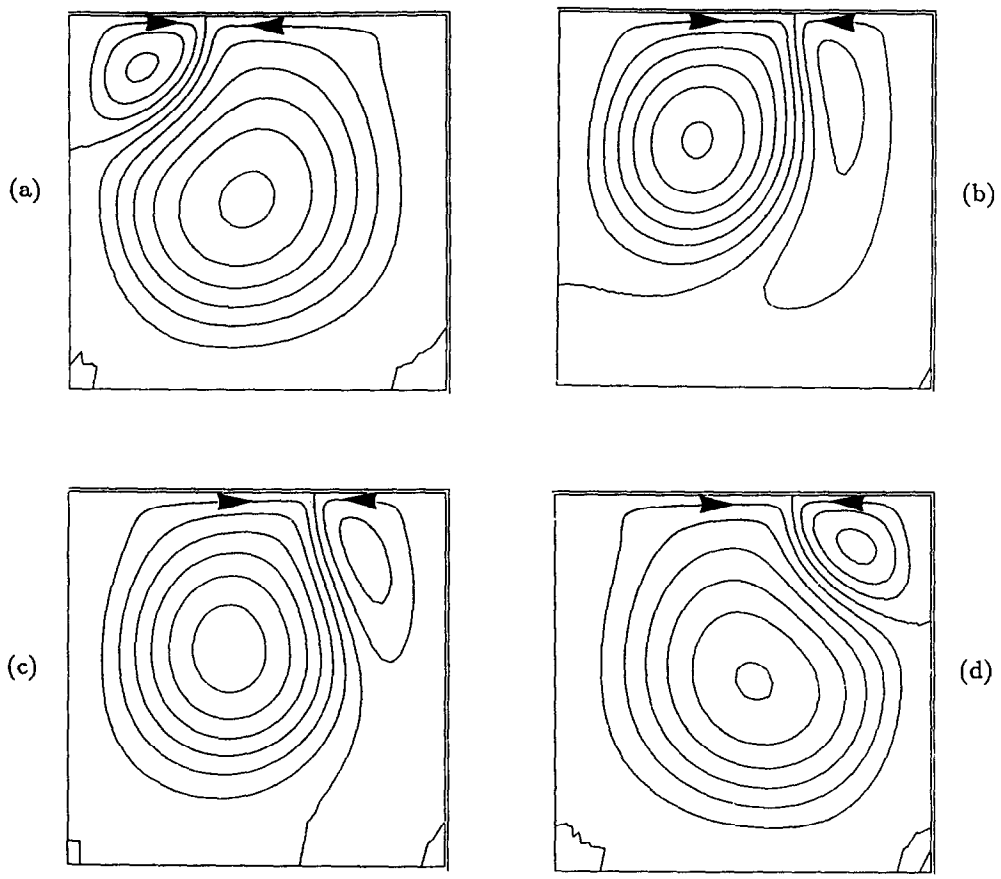

FIG. 3. Oscillating streamline contours for one half of a cycle for $Ma = 2000$. $t = 20.8$ s (a), $t = 22.2$ s (b), $t = 22.6$ s (c), $t = 23.2$ s (d). Streamline contours are in increments of 3.17×10^{-4}.

left vortex at a maximum size and the right vortex at a minimum size, the mirror image of the state shown in Fig. 3(a). Following the state shown in Fig. 3(d), the process is reversed and the system returns to the state shown in Fig. 3(a) which completes one full cycle.

Figure 4 shows several variables starting from the initial stagnant conditions (with $Ma = 2000$) and developing to a steady state and the development of oscillations following the perturbation at $t = 2$ s. Figure 4(a) shows the location of the intersection of the dividing streamline with the top surface, X_0^*. The value of X_0^* indicates the relative sizes of the vortices, e.g. when X_0^* is close to unity the right vortex is small and the left vortex is large. Figure 4(b) shows the values of the stream function at the centers of the left and right vortices, ψ_L^* and ψ_R^*, respectively. These give the volume flow rates of the two vortices. Figure 4(c) shows the extreme values of the fluid velocity on the upper surfaces of the left and right vortices, V_L^* and V_R^*, respectively. The temperature on the surface, at $x^* = 0.5$, is shown in Fig. 4(d). Note that as the size of a vortex increases (see X_0^*), the flow rate (see ψ_L^* or ψ_R^*) increases and the fluid velocity decreases; i.e. the increase in the flow rate of a vortex is due to an increase in the size of the vortex (and is not due to an increase in the fluid velocities within it).

The forces affecting the motion are now examined.† The thermocapillary force at the upper (free) surface on the 'left' which drives the motion of the left vortex is constant (not shown), and equal in magnitude and opposite in sign (i.e. direction) to the thermocapillary force at the upper (free) surface on the 'right' which drives the motion of the right vortex (see Appendix). There are also viscous shear forces acting on the fluid at the no-slip walls of the cavity which resist the motion of the fluid; these are given by $\mu \int \omega ds$, where s is the distance measured along the boundaries of the cavity, and are positive when leading to counterclockwise rotation and are negative when leading to a clockwise rotation. The value of the thermocapillary force is approximately twice the value of the viscous shear force acting on both vortices. The viscous shear (drag) forces acting on the left and right vortices, $\mathbf{F}_{L-visc}^*$ and $\mathbf{F}_{R-visc}^*$, respectively (the forces are scaled

† It is noted that a referee indicated that a description for why the oscillations take place may also be made in terms of vorticity or momentum conservation.

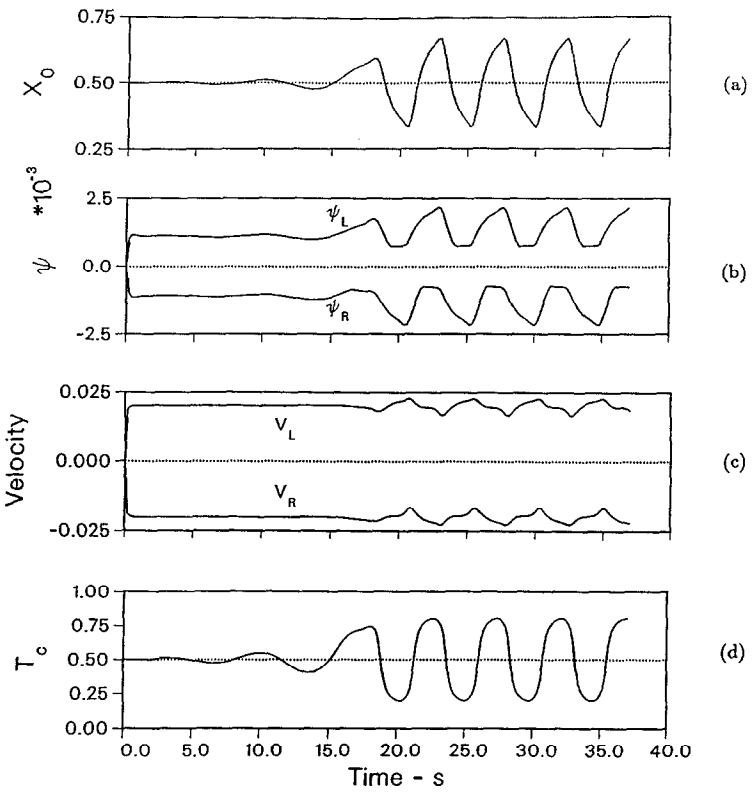

FIG. 4. The oscillating values of the location of the dividing streamline at the upper surface, X_0^* (a), the values of the stream function in the center of the left and right vortices, ψ_L^* and ψ_R^*, respectively (b), the extreme values of the fluid velocity on the upper surfaces of the left and right vortices, $\mathbf{V}_L^*$ and $\mathbf{V}_R^*$, respectively (c), and the temperature at the center of the upper surface, T_c^* (d), vs time for $Ma = 2000$.

by $\mu V_c L$), are of opposite sign (consistent with the opposite directions of rotation of the left and right vortices), and are neither equal (in absolute value) nor steady, and this inequality causes the oscillations. The sign of the net viscous shear force, $\mathbf{F}^*_{\text{net visc}} = \mathbf{F}^*_{\text{L-visc}} + \mathbf{F}^*_{\text{R-visc}}$, determines which vortex increases in volume and which decreases.

Figure 5 shows the values of $\mathbf{F}^*_{\text{L-visc}}$, $\mathbf{F}^*_{\text{R-visc}}$, $\mathbf{F}^*_{\text{net-visc}}$, $\mathbf{V}_L^*$ and $\mathbf{V}_R^*$. The velocities are shown because their direction of change, i.e. whether they are increasing or decreasing, is representative of the direction of change of the fluid velocities throughout the respective vortices. This is pertinent to the following discussion because the shear stress acting on the fluid at the no-slip boundaries increases with increasing fluid velocity. The times of the states shown in Fig. 3 are noted in Fig. 5 to help clarify the oscillations. At the time of the state shown in Fig. 3(a), labeled 'a' in Fig. 5, the left vortex has collapsed and the right vortex has completed filling most of the volume of the cavity. Although the fluid velocities in the right vortex are relatively low, as indicated by the near minimum value of $|\mathbf{V}_R^*|$, the contact area of the right vortex with the no-slip boundaries of the cavity, A_R, is large (as shown in Fig. 3(a)) which results in a large drag force. The large negative 'spike' in the curve for $\mathbf{F}^*_{\text{R-visc}}$ at the time labeled 'a' shows this large drag force. At the same time the contact area of the left vortex with the no-slip boundaries, A_L, is small. The small positive 'spike' in $\mathbf{F}^*_{\text{L-visc}}$ at the time labeled 'a' is due to the near maximum values of the fluid velocities in the left vortex. The net drag force, $\mathbf{F}^*_{\text{net-visc}}$, is negative, i.e. the value of $|\mathbf{F}^*_{\text{R-visc}}|$ is larger than that of $|\mathbf{F}^*_{\text{L-visc}}|$, which causes the left vortex to increase in size and the right vortex to decrease.

As the size of the left vortex increases and the state of the system progresses towards that shown in Fig. 3(b), the fluid velocities in the left vortex decrease and those in the right vortex increase, and since A_R remains much larger than A_L, $\mathbf{F}^*_{\text{net-visc}}$ remains negative. This results in the continued increase in the size of the left vortex. Generally, for A_R larger than A_L, $|\mathbf{F}^*_{\text{R-visc}}|$ will be larger than $|\mathbf{F}^*_{\text{L-visc}}|$ and the left vortex continues to increase in size. Note, however, that at the time labeled 'c' in Fig. 5, the right vortex begins to collapse as shown in Fig. 3(c). Here A_L is larger than A_R, but the flow field in the left vortex near the bottom of the cavity is still developing and the fluid velocities there are relatively small at this time. Hence the additional contact between the left vortex with this portion of the no-slip boundary has not yet resulted in an important contribution to $\mathbf{F}^*_{\text{L-visc}}$. Thus $|\mathbf{F}^*_{\text{R-visc}}|$ remains larger than $|\mathbf{F}^*_{\text{L-visc}}|$ and the collapse of the right vortex continues. At the time labeled 'd' in Fig. 5, where the right

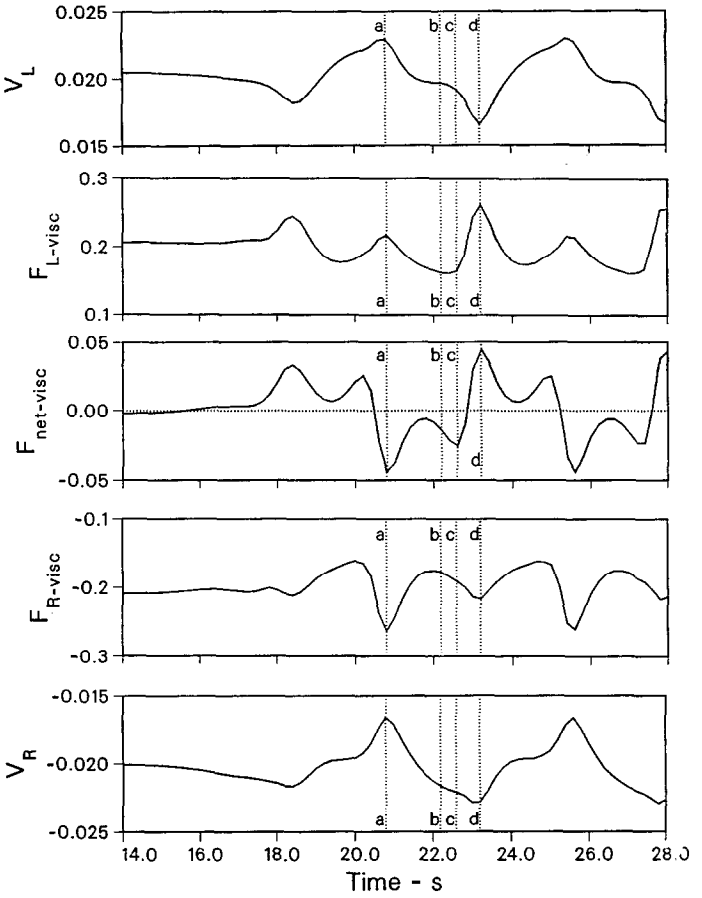

FIG. 5. The extreme values of the fluid velocity on the upper surfaces of the left and right vortices, $\mathbf{V}_L^*$ and $\mathbf{V}_R^*$, respectively. The oscillating values of the viscous shear forces acting on the fluid at the no-slip boundaries for the left and right vortices, $\mathbf{F}_{L-visc}^*$ and $\mathbf{F}_{R-visc}^*$, respectively, and the net viscous shear force, $\mathbf{F}_{net-visc}^* = \mathbf{F}_{L-visc}^* + \mathbf{F}_{R-visc}^*$, for $Ma = 2000$.

vortex has fully collapsed (Fig. 3(d)), the state of the system is the mirror image of that discussed for the time labeled 'a'. There is a large positive 'spike' in $\mathbf{F}_{L-visc}^*$ due to both the large value of A_L and the large velocities in the vicinity of the no-slip boundaries. This results in a value of $|\mathbf{F}_{L-visc}^*|$ which is larger than $|\mathbf{F}_{R-visc}^*|$ (i.e. a positive value of $\mathbf{F}_{net-visc}^*$) and now the right vortex begins to increase in size. Thus, it is the collapse of the right (or left) vortex that results in a change in sign of $\mathbf{F}_{net-visc}^*$ which then initiates its re-growth.

Calculations were carried out for intermediate values of Ma in order to identify more precisely the critical value of the Marangoni number, Ma_c. The effects of large perturbations on the flow for $Ma = 1125$ diminished with time, as discussed for the $Ma = 1000$ case, except that now more time was required for the flow to return to a steady state. Perturbations for $Ma = 1250$ and 1500 resulted in periodic oscillations in the flows, and a value of Ma_c of approximately 1200 is suggested. For those cases where the perturbation resulted in an oscillating flow, the amplitude and frequency of the oscillations increased with increasing values of Ma.

Note that in the cases discussed above, the maximum value of the surface tension was near the center of the surface and the direction of flow near the surface was towards this central location. The opposite case was also considered, i.e. the maximum value of the surface tension was located at the walls, i.e. $\gamma^* = 0.25 - T^* + T^{*2}$. This resulted in two counter rotating vortices, as obtained for γ^* given by equation (9a), except that for this case the directions of rotation were counter-clockwise for the left vortex and clockwise for the right vortex, i.e. the flow was outwards from the center of the free surface towards the left and right walls. The flow was stable for all values of Ma considered which included values for Ma up to 10 000.

5. SUMMARY AND CONCLUSIONS

Thermocapillary flow in a differentially heated two dimensional square cavity was studied for a fluid containing impurities such that the surface tension was a quadratic function of the temperature and $Pr = 0.1$. For Ma greater than approximately 1200, the flow was found to be unstable to two dimensional asymmetric

disturbances which result in oscillations. The essential characteristic which produces the oscillations is the existence of a maximum surface tension that is near the center of the surface which results in opposing vortices where the flow direction at the surface is towards the center of the domain. This condition occurred in this study due to a surface temperature gradient that was entirely in one direction, i.e. from the cold to the hot wall, combined with positive values for $d\gamma/dT$ near the cold wall and negative values of $d\gamma/dT$ near the hot wall (which results from the presence of impurities, cf. Sahoo *et al.* [8]). This condition could also occur due to values of $d\gamma/dT$ which are entirely positive combined with a temperature gradient that is positive in the direction pointing away from the solid boundaries of the domain. This condition for the temperature would result when a heat source is applied at or near the center of the top surface and the boundaries of the domain are kept relatively cool, as occurs in weld pools. Again, a positive value of $d\gamma/dT$ is required which results, at least for a limited temperature range, from the presence of impurities.

REFERENCES

1. D. T. J. Hurle, E. Jakeman and C. P. Johnson, Convective temperature oscillations in molten gallium, *J. Fluid Mech.* **64,** 565–576 (1974).
2. D. Schwabe and A. Scharmann, Some evidence for the existence and magnitude of a critical Marangoni number for the onset of oscillatory flow in crystal growth melts, *J. Crystal Growth* **46,** 125–131 (1979).
3. C.-H. Chun and W. Wuest, Thermal Marangoni convection, *COSPAR: Space Research* (Edited by M. J. Rycoft), Vol. 19, pp. 559–562. Pergamon, Oxford (1979).
4. C.-H. Chun and W. Wuest, Experiments on the transition from the steady to the oscillatory Marangoni-convection of a floating zone under reduced gravity effect, *Acta Astronautica* **6,** 1073–1082 (1979).
5. Y. Kamotani, S. Ostrach and M. Vargas, Oscillatory thermocapillary convection in a simulated floating-zone configuration, *J. Crystal Growth* **66,** 83–90 (1984).
6. M. K. Smith and S. H. Davis, Instabilities of dynamic thermocapillary liquid layers, *J. Fluid Mech.* **132,** 119–144 (1983).
7. B. M. Carpenter and G. M. Homsy, High Marangoni number convection in a square cavity: Part II, *Phys. Fluids A* **2**(2), 137–149 (1990).
8. P. Sahoo, T. DebRoy and M. J. McNallan, Surface tension of binary metal—Surface active solute systems under conditions relevant to welding metallurgy, *Met. Trans. B* **19B,** 483–491 (1988).
9. A. Zebib, G. M. Homsy and E. Meiburg, High Marangoni number convection in a square cavity, *Phys. Fluids* **28**(12), 3467–3476 (1985).
10. G. D. Raithby and K. E. Torrance, Upstream-weighted differencing schemes and their application to elliptic problems involving fluid flow, *Comput. Fluids* **2,** 191–206 (1974).

APPENDIX

It is not immediately apparent that the net driving force is constant. The thermocapillary force, as given by equation (8b), can also be expressed in terms of the rate of change of the surface tension with distance along the free surface, $-d\gamma^*/dx^*$. The net thermocapillary force is given by the integral,

$$\int -\frac{d\gamma^*}{dx^*}dx^* = \int -d\gamma^*,$$

where the limits of integration are from $x^* = 0$ to X_0^* for the thermocapillary force driving the left vortex, $\mathbf{F}^*_{L-\gamma}$, and are from $x^* = X_0^*$ to 1 for the thermocapillary force driving the right vortex, $\mathbf{F}^*_{R-\gamma}$. The surface tension at the walls (i.e. $x^* = 0$ and 1) is zero as given by equations (5c), (6c) and (9a). The calculations show that the surface tension at $x^* = X_0^*$ is the maximum value, $\gamma^* = 0.25$, regardless of the value of X_0^*; i.e. the results for temperature at $x^* = X_0^*$, give $T^* = 0.5$ (to within 1.2% for $Ma = 2000$), which yields $\gamma^* = 0.25$. Thus, $\mathbf{F}^*_{L-\gamma} = -\mathbf{F}^*_{R-\gamma} = -0.25$, i.e. $\mathbf{F}^*_{L-\gamma}$ and $\mathbf{F}^*_{R-\gamma}$ are constant (independent of time) and equal in magnitude but with opposite sign. This is expected because the fluid everywhere on the surface flows towards the point of maximum surface tension. By definition, the point at $x^* = X_0^*$ is where the horizontal component of the fluid velocity, u, is zero with $u > 0$ (flow is in positive x-direction) for $x^* < X_0^*$ and with $u < 0$ for $x^* > X_0^*$.